Journal of Biomechanics 86 (2019) 183–192

Contents lists available at ScienceDirect

Journal of Biomechanics

journal homepage: www.elsevier.com/locate/jbiomech
www.JBiomech.com

Unlocalized crack initiation and propagation in staggered biomaterials

Yi Yan, Akihiro Nakatani *

Department of Adaptive Machine Systems, Graduate School of Engineering, Osaka University, 2-1 Yamadaoka, Suita, Osaka 565-0871, Japan

ARTICLE INFO

Article history:
Accepted 9 February 2019

Keywords:
Computational mechanics
Biomaterial
Nacre
Finite element method
Fracture
Cohesive zone model
Toughness
Crack
Stability

ABSTRACT

Many types of tissues in living organisms exhibit a combination of different properties to fulfil their mechanical functions in complex environments. Nacre with more than 90% brittle and hard phase and a little protein matrix, exhibits high strength and toughness, which is difficult to achieve in artificial materials. Researchers have shown that the toughness of nacre is related to the cracking process. Most of them, however, assume an obvious pre-existing crack on the model and the initiation of the microscopical pre-existing crack is not considered yet. Based on fracture mechanics with the cohesive zone model, we reveal the mechanism of the crack initiation and propagation pattern in staggered biomaterials without any pre-existing crack. The simulation result shows that there are two crack propagation modes: localized mode and unlocalized mode. A crack initiates and propagates in a small area in the localized mode, while cracks initiate at different points and propagate in various paths in the unlocalized mode. The crack initiation mechanism from the intrinsic properties of the material is clarified using energy based stability analysis. The result shows that the shear interfacial mechanism significantly delays the crack initiation.

1. Introduction

Some biomaterials, such as nacre, bone, and enamel are known for their high strength, toughness, and stiffness. An attractive characteristic of nacre is its significant toughness as well as strength. It has a high fracture strength and high stiffness compared to materials of other hard-soft phase ratios (from 9:1 to 1:1) (Mayer, 2006). It has also been reported that its fracture toughness is 40 times higher than the toughness of pure hard-phase materials (Wegst et al., 2014). These findings in the biomaterial inspire the possibility of artificial synthesis of materials with comprehensively high mechanical properties (Munch et al., 2008; Launey et al., 2009; Allison et al., 2015).

Recently, some researchers showed that the cracking mechanism plays an important role in the high toughness of nacre (Munch et al., 2008). The most representative quantitative discussion of the cracking mechanism is the 'rising resistance-curve', which shows that the toughness of a biomaterial increases with the crack propagation process (Launey et al., 2010; Wang and Gupta, 2011). There are also many evidences of an inelastic crack free zone in the vicinity of the notch top (Wang and Gupta, 2011; Barthelat et al., 2007), which contains micro-cracking (Launey et al., 2009; Abraham, 2001), crack deflection, and crack bifurcation (Yahyazadehfar and Arola, 2015) at a small scale. To explore the intrinsic relationship between the cracking behavior of nacre and its toughness, most of the previous studies have been based on the conventional fracture mechanics in which pre-existing cracks were assumed on the model (Shao et al., 2014; Dutta and Tekalur, 2014; Xie and Yao, 2014). Bargmann et al. (2013) and Scheider et al. (2013) deal with the model without any pre-existing cracks, but they mainly focus on the breaking mechanisms due to the microstructure of materials. Chintapalli et al. (2014) try to explain the transition mechanism from unlocalized mode to localized mode of micro-cracking in nacre. The explanation is mainly based on strain rate dependency such as viscosity of the material.

An initial crack is needed for the linear elastic fracture mechanics (LEFM). Elices et al. (2002), however, points out that LEFM is not necessarily useful for solving fracture problems due to micro-cracking in which the size of nonlinear zone is not negligible in comparison with other dimensions of the cracked geometry. The micro-cracks in nacre are observed by Barthelat and Espinosa (2007), and are believed to be strongly related with its toughening mechanisms. In this study, we successfully solve the fracture problem due to micro-cracking in nacre using the model without any pre-existed crack.

As a stability losing process, the crack initiation is related with the convexity change of the overall strain energy functional. It has some chaotic features by which the crack is triggered by some

* Corresponding author.
E-mail address: nakatani@ams.eng.osaka-u.ac.jp (A. Nakatani).

https://doi.org/10.1016/j.jbiomech.2019.02.003
0021-9290/

infinitesimal factors. This feature makes it difficult to explore the detailed mechanism of crack initiation, such as finding the cracking position in the absence of obvious pre-existing crack. In this study, we show that cracks still initiate even without any pre-existing crack. We have found two different crack patterns in the model of the staggered biomaterial inspired by nacre: localized mode and unlocalized mode. The inner mechanism of the crack initiation is analyzed in detail using stability theory, and it is shown that the shear interfacial mechanism significantly delays the global unstable point. We also provide the vital clues on the bifurcation point of the two cracking modes. Systematic research, concerning the two modes' characteristics, mathematical description, mechanical properties, inner mechanism, and affecting factors, is presented.

This paper is organized into the following sections. In Section 2, the two-dimensional theoretical model and its numerical form are introduced. A semi-analytical model composed of cohesive springs is introduced to describe the stability evolution of the system and the strain concentration associated with the crack initiation process. The key parameters of the analysis are also presented in this section. In Section 3, we introduce the concept of the two cracking modes: localized mode and unlocalized mode. The characteristics and mathematical descriptions of the two modes are presented, and the dynamic mechanical properties of the cracking process is analyzed. The vital clues on the bifurcation point of the two cracking modes are presented. Finally, we give the conclusions.

2. Model and method

2.1. Model of nacre and problem

Nacre consists of a hard aragonite phase and a soft collagen phase organized in a staggered manner. Inspired by nacre, we focus on the staggered materials, which contain the hard phases, soft phases, and interfaces, subject to tensile loading. The hard phase and soft phase are simplified as isotropic elastic solids. The basic equations of displacement u_i, stress σ_{ij}, and strain ε_{ij} in the body $\Omega \setminus \Sigma$, which is the domain except for cohesive zone Σ, are as follows. The linear balance of momentum can be reduced into the following balance equation in dynamic analysis:

$$\rho \ddot{u}_i = \frac{\partial \sigma_{ij}}{\partial x_i} + \rho g_i \quad \text{in} \quad \Omega \setminus \Sigma, \tag{1}$$

where the double dots indicate the second time derivative of displacement u_i. ρ represents the density and g_i is a component of the body force. For a static problem that does not consider any body force, the balance equation can be written as

$$\frac{\partial \sigma_{ji}}{\partial x_i} = 0 \quad \text{in} \quad \Omega \setminus \Sigma. \tag{2}$$

The boundary conditions of specified traction to t_i^0 on a surface is given by S_f

$$t_i = \sigma_{ij} n_j = t_i^0 \quad \text{on} \quad S_f, \tag{3}$$

and the specified displacement u_i to u_i^0 on surface S_u is given by

$$u_i = u_i^0 \quad \text{on} \quad S_u. \tag{4}$$

Fig. 1(a) shows the model used in the analysis. The model consists of the hard phases (blue parts), which are arranged in a staggered manner, and soft phases (green parts) which are filled between hard phases. The black and red springs represent the cohesive zone where the cracks will develop in a rectangular specimen under a specified tensile displacement loading. The traction on the boundary surface with the relative displacement (separation) represents the cohesive law on the interface Σ, on which

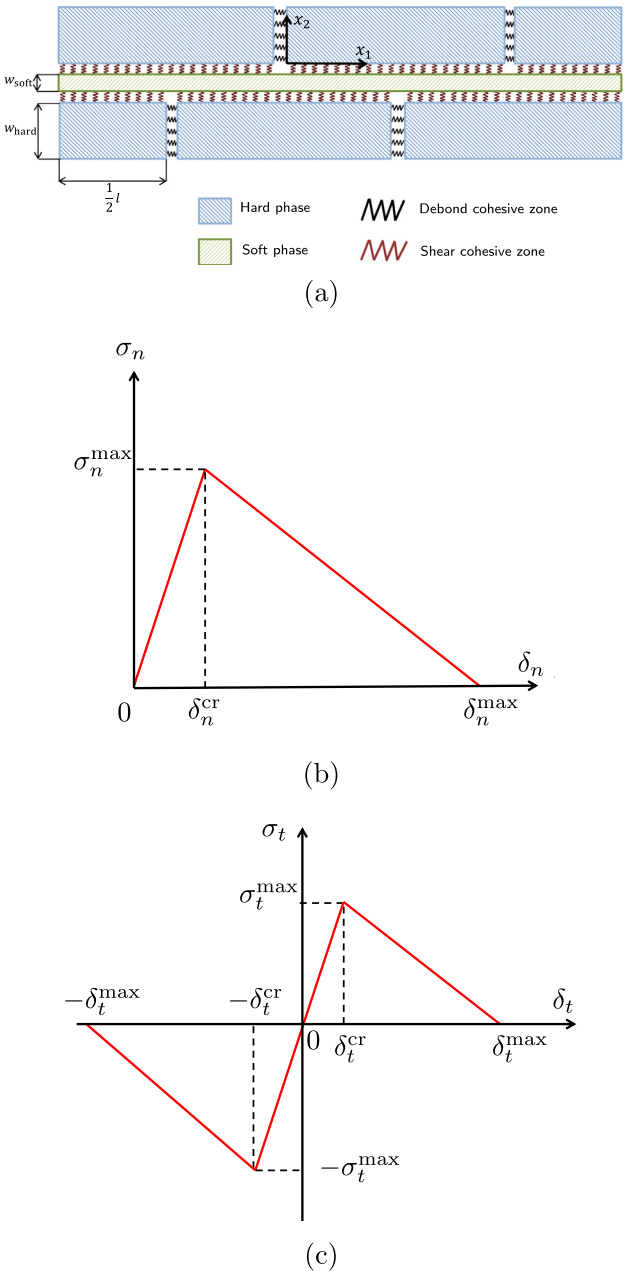

Fig. 1. Analysis model: (a) sketch of the two-dimensional model, (b) debond cohesive law, (c) shear cohesive law.

the bilinear relationships between the traction and the relative discontinuous displacement consisting a linear stiffening stage and a linear softening stage are supposed, as shown in Fig. 1(b) and (c).

2.2. Cohesive zone model

We assume that the cohesive zone relationship describes the interface behavior between the hard phase and soft phase, which is also the origin of crack initiation.

Owing to its adaptability in dealing with the interface cracking problem and its compatibility with finite element application, cohesive zone model (CZM) is widely used in researches of biomaterials (An et al., 2014a,b; Bargmann et al., 2013; Borovik and Borovik, 2014; Dastjerdi et al., 2012; He and Li, 2012; Shao et al., 2014; Scheider et al., 2015, 2013). CZM can be thought as a supplement of the fracture mechanics (Needleman, 2013). Instead of

using a single parameter such as stress intensity factor, CZM uses a set of traction-separation relationships to describe the dynamic cracking process. It usually has a stiffening stage (positive modulus) and a softening stage (negative modulus). No pre-existing crack is needed but only to specify a 'crack propagation route' using CZM so that it is suitable for the material in which cracks generally exist at the interface.

The discontinuous jump of displacement on the interface Σ, which is a thin layer between two surfaces in a three-dimensional model or a thin path in a two-dimensional model,

$$[\![\boldsymbol{u}]\!] = u^+ - u^- \quad \text{on} \quad \Sigma \tag{5}$$

is taken into account, where u^+ and u^- are the limits of the value of displacement between both sides of the interface Σ.

The normal component δ_n and the tangential component δ_t are derived by

$$\delta_n = [\![\boldsymbol{u}]\!] \cdot \boldsymbol{n}, \quad \delta_t = [\![\boldsymbol{u}]\!] \cdot \boldsymbol{t}, \tag{6}$$

where $\boldsymbol{n}$ and $\boldsymbol{t}$ are the normal and tangential unit vectors of the interface surface.

In general, there is some covariation between the normal and tangential cohesive laws. For simplicity, we give the overall cohesive potential $\phi(\delta_n, \delta_t)$ as

$$\phi(\delta_n, \delta_t) = \phi_n(\delta_n) + \phi_t(\delta_t). \tag{7}$$

To separate the two cohesive mechanisms further, we give subscripts n and t corresponding to the quantities for debond cohesive zone and shear cohesive zone, respectively, which reflects the two kinds of interfaces as shown in Fig. 1(a).

Then, in the cohesive zone model, the normal and shear components of traction, σ_n and σ_t, respectively, are given by

$$\sigma_n = \frac{\partial \phi}{\partial \delta_n} = \frac{d\phi_n}{d\delta_n} = f_n(\delta_n), \quad \sigma_t = \frac{\partial \phi}{\partial \delta_t} = \frac{d\phi_t}{d\delta_t} = f_t(\delta_t). \tag{8}$$

The cohesive functions $f_n(\delta_n)$ and $f_t(\delta_t)$ are generally nonlinear. In this study, however, simple bilinear forms are considered, in which $\phi_n(\delta_n)$ and $\phi_t(\delta_t)$ are given by

$$\phi_n(\delta_n) = \begin{cases} \frac{1}{2} k_n \left(\delta_n^2 - \delta_n^{\mathrm{cr}} \delta_n^{\max}\right) & \left(\delta_n < \delta_n^{\mathrm{cr}}\right) \\ -\frac{1}{2}\left(\frac{\delta_n^{\mathrm{cr}}}{\delta_n^{\max} - \delta_n^{\mathrm{cr}}}\right) k_n \left(\delta_n - \delta_n^{\max}\right)^2 & \left(\delta_n^{\mathrm{cr}} < \delta_n < \delta_n^{\max}\right) \\ 0 & \left(\delta_n > \delta_n^{\max}\right) \end{cases} \tag{9}$$

and

$$\phi_t(\delta_t) = \begin{cases} \frac{1}{2} k_t \left(\delta_t^2 - \delta_t^{\mathrm{cr}} \delta_t^{\max}\right) & \left(|\delta_t| < \delta_t^{\mathrm{cr}}\right) \\ -\frac{1}{2}\left(\frac{\delta_t^{\mathrm{cr}}}{\delta_t^{\max} - \delta_t^{\mathrm{cr}}}\right) k_t \left(|\delta_t| - \delta_t^{\max}\right)^2 & \left(\delta_t^{\mathrm{cr}} < |\delta_t| < \delta_t^{\max}\right) \\ 0 & \left(|\delta_t| > \delta_t^{\max}\right) \end{cases} \tag{10}$$

This simplest relationship is described by three parameters. Various literatures have mentioned that the cohesive interfacial properties are mainly dependent on two of them: maximum stress $\sigma^{\max}$ and total energy U^{total} (Shao et al., 2012; Tvergaard and Hutchinson, 1992; Barthelat et al., 2007). This study adopts the parameter of $\sigma^{\max} = 30$ MPa from Shao et al. (2012) and $U^{\mathrm{total}} = 1575\ \mathrm{J/m^2}$ from Wegst and Ashby (2004).

The maximum traction $\sigma_n^{\max}, \sigma_t^{\max}$ is evaluated as follows:

$$\sigma_n^{\max} = k_n \delta_n^{\mathrm{cr}}, \quad \sigma_t^{\max} = k_t \delta_t^{\mathrm{cr}}, \tag{11}$$

where k_n and k_t represent the cohesive stiffness in the stiffening stage, which has a different dimension than the Young's modulus.

The strain energy of the cohesive zone $U^{\mathrm{coh}}(\delta_n, \delta_t)$ is given by

$$U^{\mathrm{coh}}(\delta_n, \delta_t) = \phi_n(\delta_n) + \phi_t(\delta_t) + \frac{1}{2}\left\{k_n \delta_n^{\mathrm{cr}} \delta_n^{\max} + k_t \delta_t^{\mathrm{cr}} \delta_t^{\max}\right\}. \tag{12}$$

We consider two reasons for choosing the simplest bilinear cohesive relationship. First, the bilinear cohesive relationship describes the main stream of the interfacial properties. In this study, the interfacial behavior is classified into 'debond' and 'shear' cohesive zones. The bilinear cohesive relationship is well coherent with the molecular dynamics simulation of the debonding process of the vertical interface in nacre-like biomaterials (Dubey and Tomar, 2009b). The softening process is related to the dynamic failure of protein adhesion, and originate from some complicated deformation mechanisms of the soft phase such as the molecular rotation, H-bond rupture, and back bone stretching (Gautieri et al., 2009). The sliding behavior of the horizontal interface leads to a reduction of adhesion area, which further leads to interfacial softening. In addition, the simple cohesive relationship helps us reduce the affecting parameters, and better understand the inner mechanisms of solution mode transition.

Actually, the interfacial behavior of nacre is complicated, and involves several mechanisms such as the adhesion between soft and hard phases, nano-asperities, and mineral bridges (Askarinejad and Rahbar, 2015). These mechanisms can be taken into account by considering the shape of the cohesive constitutive relationship, which can be derived from calculations at a deeper level (Cho and Park, 2004; Jiang, 2010).

2.3. Stability evolution and strain concentration in cohesive spring system

In this study, we focus on the interfacial crack initiation process, which can be considered as the mechanical response of a cohesive spring system. The critical displacements δ_n^{cr} and δ_t^{cr} in Fig. 1(b) and (c) define the points from a locally stable stage to a locally unstable stage. However, for the cohesive spring system rather than a single spring, the local instability causes something unique that happens globally; this is called 'strain concentration' in this study.

First, a system composed of only four debond cohesive springs (1), (2), (3), and (4) in series is taken into account as shown in Fig. 2. Suppose a displacement loading Δ is given on its end. Then, the elongation δ_i of spring (i) $(i = 1, \cdots, 4)$ satisfies

$$\sum_{i=1}^{4} \delta_i = \Delta, \tag{13}$$

and the force equilibrium

$$F(\delta_1) = F(\delta_2) = F(\delta_3) = F(\delta_4) \tag{14}$$

is satisfied, where $F(\delta)$ is the cohesive traction as a function of relative displacement δ. In the case of low loading, all of the springs share the same deformations and reactive forces, which refers to the fully elastic stage. When the elongation of the springs exceeds the critical displacement, the system has multiple solutions for equilibrium, i.e., the states of the springs can evolve to the softening stage as well as shrink back to the stiffening stage. The model shown in Fig. 2 can be regarded as a simplification of the model of nacre without the shear cohesive zone. Actually, we have calculated the mechanical response of the model shown in Fig. 1 by considering only debond cohesive zone. The result shows a completely localized crack mode with only one spring in the softening stage and the others shrinking back to the stiffening stage as shown in Fig. 2(e). We must understand why the system choose the localized solution rather than the homogeneous deformations (Bigoni, 2012). Fig. 2(e) shows schematic illustrations of multiple solutions. In general, nature chooses the solution corresponding to the minimum energy among the kinematically admissible solutions, which also satisfy the statical equilibrium (Bigoni, 2012). While the solution is a stable equilibrium configuration, the others are unstable.

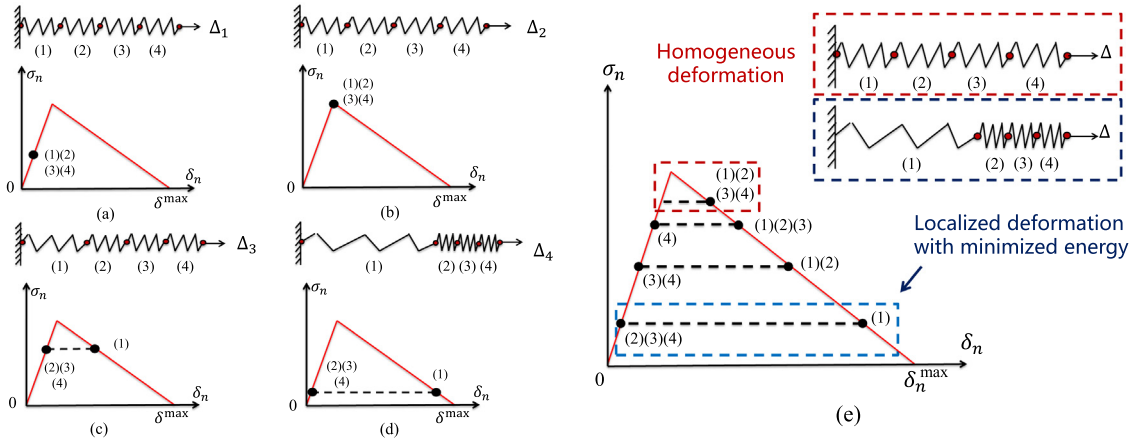

Fig. 2. A simple model of cohesive springs in series: (a–d) its strain evolution, (e) all the characteristic solutions after the bifurcation point.

Now it is known that the localized crack mode and strain concentration are the intrinsic features of a model with only debond cohesive zones. Secondly, we discuss the effect of shear cohesive zone. We introduce a model taking into account the shear cohesive zone, as shown in Fig. 3. In this model, several cohesive springs are connected in series, in which the geometrical condition is specified by Eq. (13), and other series of shear cohesive springs are taken into account. We introduce a phenomenological equation of the strain distribution in soft phase

$$\varepsilon_{11}^{\text{soft}}(x_1) = \left\{ \frac{\left(\frac{x_1}{l_r} - \frac{1}{2}\right)^k}{\left(\frac{1}{2}\right)^k} b + (a-b) \right\} \bar{\varepsilon} \tag{15}$$

to describe the distribution of relative displacement in the shear cohesive springs, where x represents the local coordinates in the representative length l_r of the soft phase, which is the minimum length needed to describe the overall strain distribution of the soft phase. The boundary conditions of relative displacements of the shear springs are specified by the half of the relevant debond spring.

In this model, $l_r = l/2$, in which l is the length of a single platelet of the hard phase. $\bar{\varepsilon}$ is the average strain in the soft phase, which can be written as $\bar{\varepsilon} = \Delta/L$, in which Δ is the displacement loading and L is the overall length of the specimen. Eq. (15) contains three parameters, k, a, and b.

Given a certain distribution of $\varepsilon_{11}^{\text{soft}}(x_1)$, the displacement in the soft phase can be written as

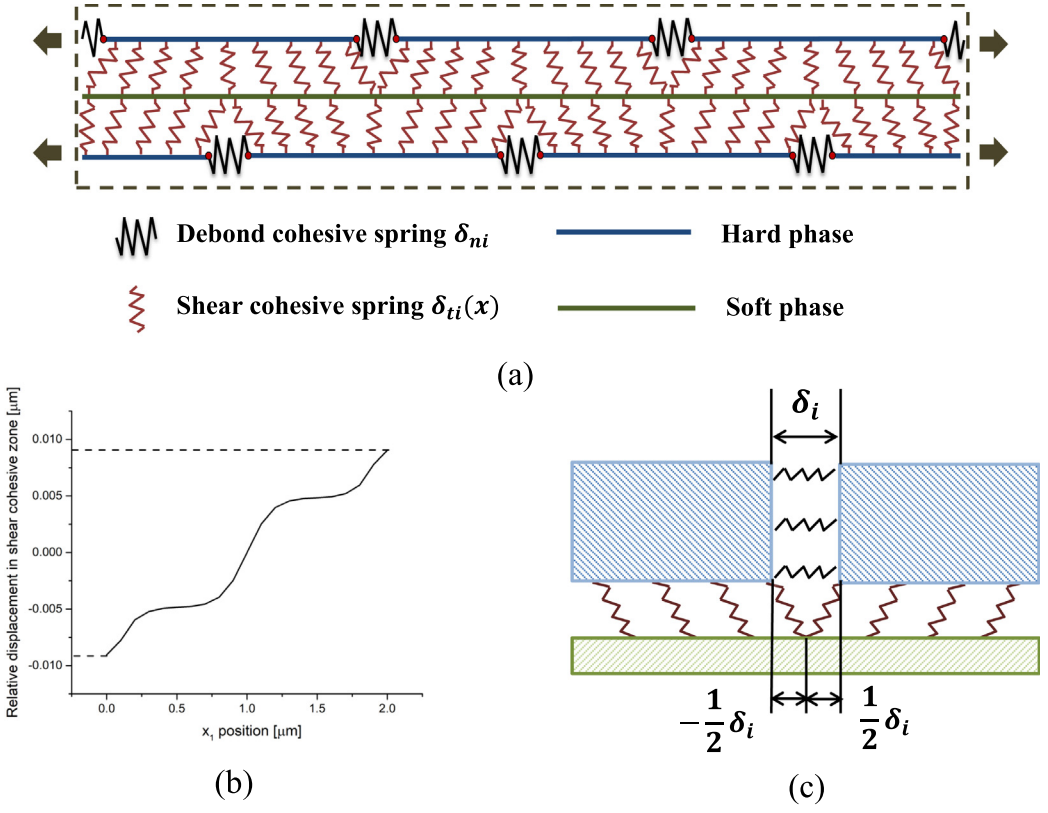

Fig. 3. Semi-analytical model for describing the separation of local and systematic instabilities: (a) sketch of 1-dimensional cohesive spring system, (b) distribution of shear cohesive separation in the x_1 direction, (c) relationship between the boundary value of (b) and the respective debond cohesive spring.

$$u_1^{\text{soft}}(x_1) = \int_0^{x_1} \varepsilon_{11}^{\text{soft}}(\xi) d\xi + u_1^{\text{soft}}(0), \tag{16}$$

where a constant $u_1^{\text{soft}}(0)$ is specified as the boundary condition value.

The cohesive separation is defined as the relative displacement at the interfaces. The tangential relative displacement on shear cohesive zone is

$$\delta_t(x_1) = u_1^{\text{soft}}(x_1) - u_1^{\text{hard}}(x_1), \tag{17}$$

where $u_1^{\text{hard}}(x_1)$ is the displacement of hard phase at x_1. Because of the much higher elastic modulus in the hard phase, the strain du_1^{hard}/dx_1 is negligibly small compared with the strain du_1^{soft}/dx_1; therefore, the relative displacement in the shear cohesive zone is determined by

$$\delta_t(x_1) = u_1^{\text{soft}}(x_1) + C_{\text{accum}}, \tag{18}$$

where C_{accum} is a constant. The tractions f_n and f_t in the debond and shear cohesive zones can be determined by the cohesive constitutive relationship, where δ_n can be calculated by the separation of the hard phases. After calculating the distribution of the relative displacement, we can estimate the strain energy of the system by

$$E_{\text{system}} = \sum_{i=1}^{n_n} f_{ni}\delta_{ni} w_{\text{hard}} + \sum_{j=1}^{n_t} \int_0^l f_{tj}(x_1)\delta_{tj}(x_1) dx_1, \tag{19}$$

where the subscripts i and j denote the values of the i-th debond and the j-th shear cohesive zone, respectively, and n_n and n_t represent the numbers of the debond and shear cohesive zones, respectively.

Here, $u_1^{\text{soft}}(0) = 0$, and we consider a special case with respect to the model with the aspect ratio $l/w_{\text{hard}} = 5, l_r = 1$, $E_{\text{hard}} = 60$ GPa, and $E_{\text{soft}} = 2.8$ GPa. Assume $k = 4, a = 4$, and $b = 3.75$.

Fig. 4 shows the total strain energy of the system. In the figure, the localized solution (red curve), which shows the evaluation of the inelastic behavior under an assumption that one debond cohesive spring is elongated more than the critical displacement while the others are still elastic, is compared with homogeneous solution (black curve) that all debond cohesive zones in the softening stage. This graph can be divided into three stages. The multiple solutions phenomenon emerges from stage I to II, when the debond cohesive zone steps into the softening stage. At this stage, however, the energy of the homogeneous solution is lower than the localized solution due to the shear cohesive zone. It indicates that the global stability of the system is still kept in a homogeneous deformation. Finally, the system turns into localized deformation in stage III.

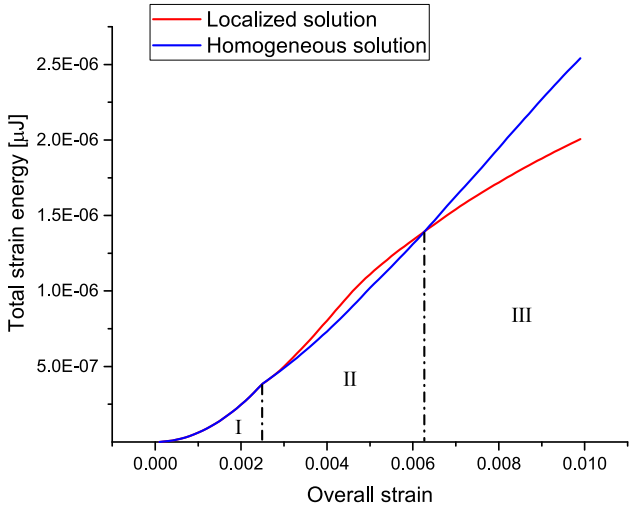

Fig. 4. Strain energy calculation of the two characteristic solutions.

We concisely summarize the key points in this section. The softening cohesive behavior leads to the strain concentration phenomenon when the cohesive spring system is considered. After the system loses its global stability, the strain rapidly concentrates to a single point, which becomes the source of the crack initiation. Taking into account the shear cohesive mechanism, the globally unstable point is separated from the locally unstable point.

2.4. Finite element analysis

The finite element simulation is conducted with the commercial software ABAQUS Explicit, 6.14. The model is almost the same as that shown in Fig. 1(a), with the constraints in the x_2-direction applied on the top and bottom boundaries of the model.

For the soft phase, previous studies mentioned several different types of mechanical responses, such as pure elastic with high modulus (PMMA), pure elastic with low modulus (PLMA), and elastic-plastic (PUA-PHEMA) with the elastic modulus varying from 0.077 MPa to 2GPa (Niebel et al., 2016). In order to simplify the model, we use the parameter of the PMMA-like material. All the geometric and material parameters are shown in Table 1.

2.5. Localization factor

In order to describe the difference between the two modes quantitatively, we raised a dimensionless parameter, localization factor, which is defined as follows:

$$L_{\text{F}} = \frac{1}{\Omega_{\text{soft}} \bar{\varepsilon}_{11}^2} \int_{\Omega_{\text{soft}}} (\varepsilon_{11} - \bar{\varepsilon}_{11})^2 dV, \tag{20}$$

where ε_{11} represents the tensile strain in the soft phase and $\bar{\varepsilon}_{11}$ represents the average strain

$$\bar{\varepsilon}_{11} = \int_{\Omega_{\text{soft}}} \varepsilon_{11} dV. \tag{21}$$

The localization factor corresponds to the square of the coefficient of variance in the statistics theory. It also refers to the strain localization in the soft phase, and a higher value indicates a higher localized crack pattern. This parameter is ill-defined in the vicinity of $\varepsilon_{11} = 0$, but it is well-defined in the inelastic cracking process, and it is effective for characterizing the heterogeneity of the cracking strain.

From the origins of strain distribution in the soft phase, we can roughly classify L_{F} into:

$$L_{\text{F}} = L_{\text{F}}^{\text{boundary}} + L_{\text{F}}^{\text{structure}} + L_{\text{F}}^{\text{localization}}. \tag{22}$$

$L_{\text{F}}^{\text{boundary}}$ represents the distribution variance resulting from the boundary effect of the system. The strain is relatively lower near the left and right boundaries of the model. This variance has a less significant physical meaning, and it does not change with the loading.

$L_{\text{F}}^{\text{structure}}$ originates from the stiffness difference among the hard phase, soft phase, and the cohesive interface as well as the staggered structure of the model, which can be roughly evaluated from Eq. (15)(see Fig. 8a).

$L_{\text{F}}^{\text{localization}}$ represents the change in the shape of distribution when strain localization occurs. It cannot be observed when the system is in the unlocalized mode. It can be roughly evaluated that $L_{\text{F}}^{\text{localization}}$ occupies about 84–91% of the L_{F} difference in the two cracking modes. Accordingly it is reasonable to conclude the validity of using the localization factor in characterizing the strain localization of this model.

Table 1
Parameters of the specimen (standard values).

Geometric parameters	Platelet width w_{hard} [nm]	Collagen width w_{soft} [nm]	Aspect ratio l/w_{hard}
	400	30	5
Material parameters	Young's modulus		Poisson's ratio
	E_{hard} [GPa]	E_{soft} [GPa]	ν_{hard} ν_{soft}
	60	2.8	0.3 0.4
Cohesive parameters	Maximum displacement $\delta_{n/t}^{max}$ [nm]	Critical displacement $\delta_{n/t}^{cr}$ [nm]	Maximum stress $\sigma_{n/t}^{max}$ [MPa]
	105	5	30

3. Results

Though nacre is famous for its ductile fracture and high toughness, many researches have mentioned the brittle fracture pattern in nacre as well as some similar materials. For example, the nacre without water shows brittle fracture that is similar to the pure hard phase (Barthelat et al., 2007), which has also attracted the attention of many researchers (Dubey and Tomar, 2009b,c,a; Ghosh et al., 2007). Some artificial nacre-like materials have shown brittle failure (Niebel et al., 2016) in mechanical tests. These experimental evidences show that there must be some factors that determine the fracture mode differentiation and this paper aims to explore these factors based on the intrinsic properties of materials.

3.1. Localized and unlocalized crack modes

In this study, we found that if the parameters in Table 1 are changed, various crack initiation and propagation patterns with completely different mechanical responses emerge. In general, they can be classified into the localized mode and the unlocalized mode. In the localized crack mode, the crack initiates in only one position and extends close to that position during the whole process. In the unlocalized mode, several different micro-cracks emerge and extend. The crack initiation and extension patterns of the two modes can be seen in Fig. 5. The contour corresponds to the strain distribution in the x_1-direction.

From the simulation result, it can be seen that the cracking process corresponds well with the failure sequence of staggered biomaterials reported by Askarinejad and Rahbar (2015, 2018), which includes debond interface failure, shear interfacial sliding and complete pull-out.

3.2. Quantitative characterization

The stress-strain curves and evolution of the localization factor of the two modes are shown in Fig. 6(a) and (b), respectively.

In Fig. 6(a), the localized mode shows a brittle mechanical response and the unlocalized mode shows a ductile mechanical response. In the localized crack mode, the stress rapidly increases to a high value at the beginning and then shows an abrupt drop. With the crack propagation, the stress rises again but undergoes a huge fluctuation till the complete detachment of the platelets. In the unlocalized crack mode, the stress increases nonlinearly and reaches a lower maximum value. When the crack initiates, the stress drops a little and then rises again smoothly. It should

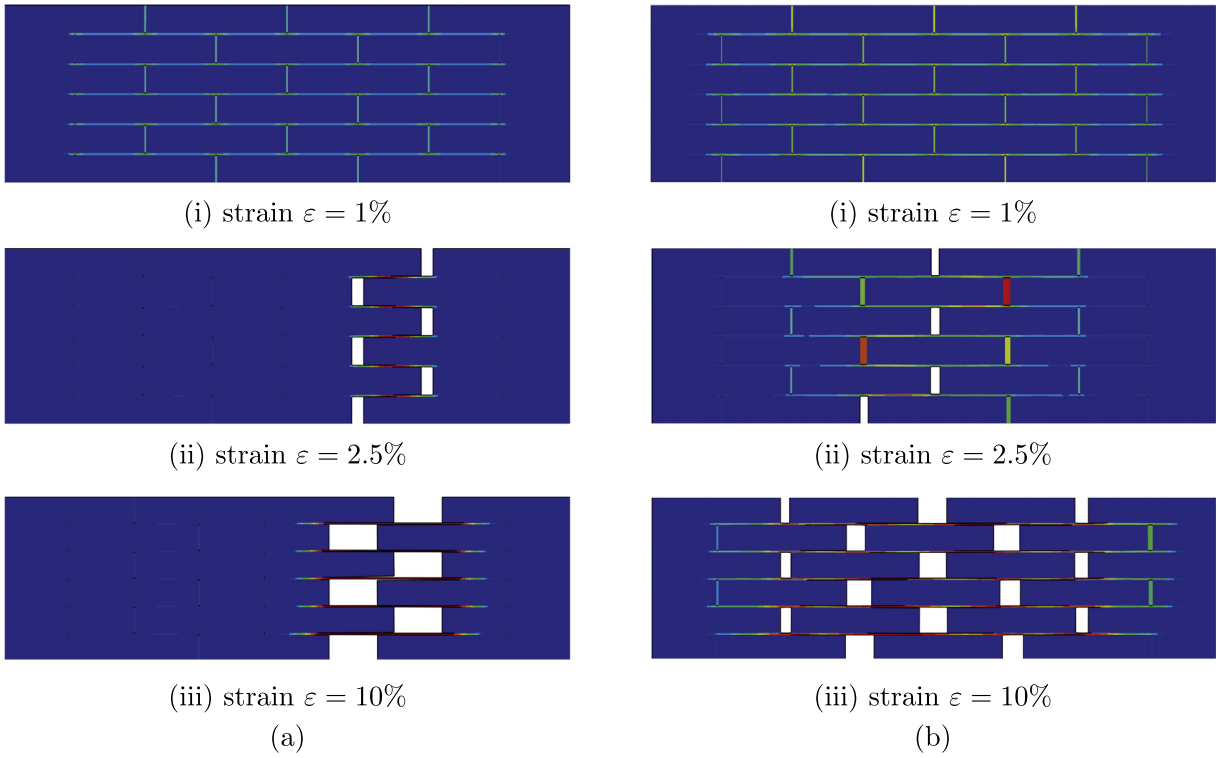

Fig. 5. Crack pattern by FEA: (a) localized mode (all parameters in standard value), (b) unlocalized mode ($E_{soft} = 11.2$ MPa, others in standard value).

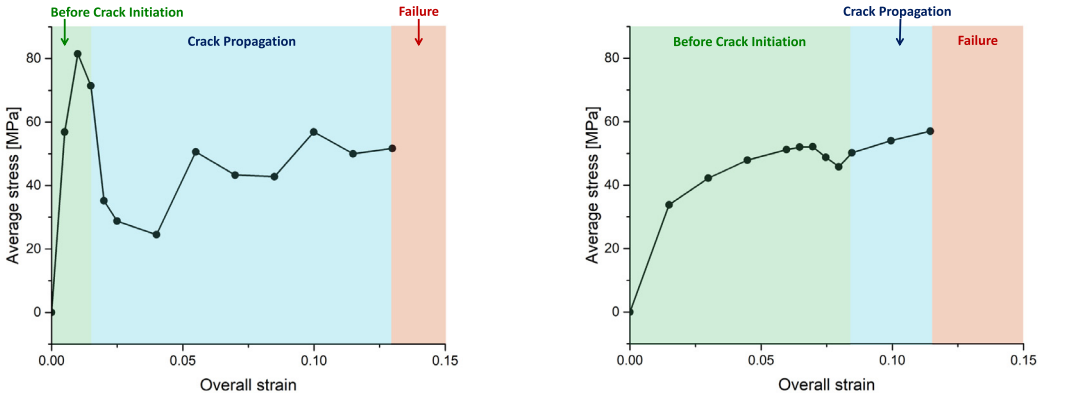

(i) localized mode (standard value) (ii) unlocalized mode (aspect ratio $l/w_h = 1$)

(a) stress-strain relationship

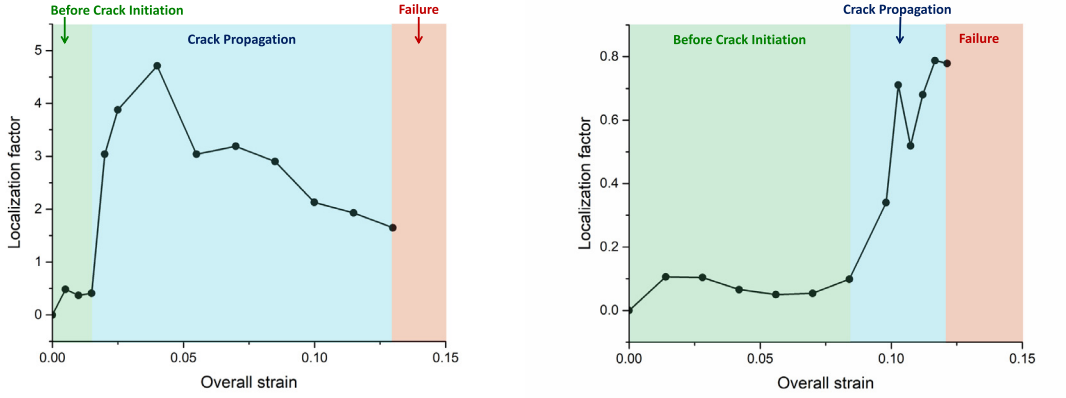

(i) localized mode (standard value) (ii) unlocalized mode (aspect ratio $l/w_h = 1$)

(b) localization factor vs. strain relationship

Fig. 6. Overall properties of the localized and unlocalized modes depending on the aspect ratio of the hard phases: (a) stress-strain curve, (b) localization factor vs. strain.

be noted that the stress reaches the maximum value just before the crack initiation in the two modes. It shows that the crack mode differentiation begins before the emergence of the first free surface. The change that happens in this brief period will be the focus of the discussion in the next section.

In Fig. 6(b), we can see that the factor depicts inhomogeneity in each mode. Two modes, however, have completely different L_F values. In both modes, the localization factor is low before the crack initiation, and has an abrupt increase at the time of the crack initiation. After the crack initiation, the localization factor soon reaches the maximum value and then decreases slowly. However, the localized crack mode has a much higher localization factor than the unlocalized mode. This shows that the localized mode has a more severe strain localization when the crack initiates.

3.3. Inner mechanism of the crack mode differentiation

In this section, we will concisely discuss the intrinsic mechanism of the crack mode differentiation using a specific and representative example. In the previous section we have shown the crack initiation and propagation process of the two crack modes in Fig. 5. A critical phenomenon must be noticed comparing with Fig. 5(a)(i) and (b)(i). At the beginning stage, the strain distribution is homogeneous and the two modes behave almost the same, but after a critical point, the crack initiates remarkably and the strain distribution becomes macroscopically inhomogeneous. We call this point the bifurcation point from the macroscopically homogeneous to inhomogeneous deformation. To show this bifurcation point more clearly, Fig. 7 illustrates the strain evolution of the debond cohesive elements. It shows that the bifurcation point with about 1% overall strain exists in both the crack modes. Before the bifurcation point, the strain evolutions are macroscopically homogeneous in both modes. After it, however, the state of strain distribution of the two modes apparently varies. In the localized mode, the strain bifurcates into two branches. One of them refers to the strain in the cracking zone while the other one refers to the non-cracking positions. In the unlocalized mode, the strain distributes inhomogeneously, but rather evenly, which also indicates the crack initiation all over the specimen.

From Fig. 7 we know that there exists an apparent gap between the global bifurcation point and the local critical point in the cohesive relationship. However, in these two specimens, when E_{soft} is changed, the global bifurcation points are the same but they still show different behaviors after the bifurcation point. Accordingly, it is necessary to find what actually happened at the global bifurcation point and which factor determines the crack mode differentiation.

Fig. 8(a) and (b) show the strain distribution of the soft phase in the loading direction and the strain distribution on the shear cohesive zone at the bifurcation point, respectively. In Fig. 8(a), it is shown that though the average strains of the two models are almost the same, the distribution differs. Because of the lower elas-

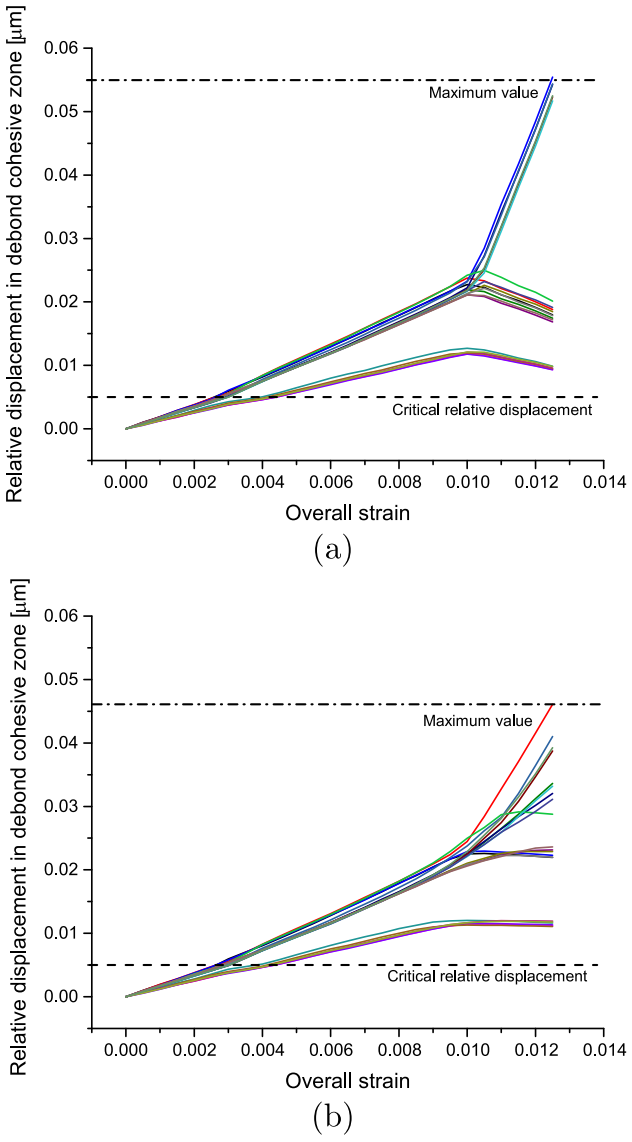

Fig. 7. Relative displacement δ_n evolution of debond cohesive elements: (a) localized crack mode (default setting), (b) unlocalized crack mode ($E_{soft} = 11.2$ MPa).

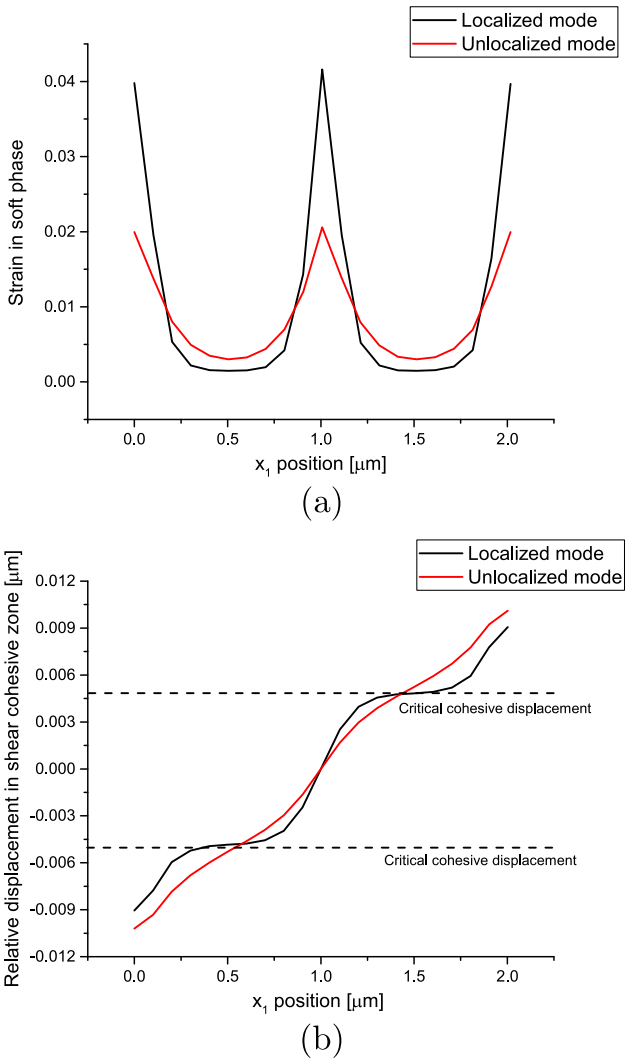

Fig. 8. Localized mode with standard parameters and unlocalized mode with $E_{soft} = 11.2$ GPa: (a) strain distribution of the soft phase in the x_1-direction, (b) distribution of the relative displacement in the shear cohesive zone at the bifurcation point.

tic modulus in the localized crack model, the strain concentration is more severe than the unlocalized crack model. It is noticed that in the localized crack model, there exists a long plateau area in which the strain distribution is flat and near to zero. We call it the constant strain area. The existence of the constant strain area in the localized crack model is the most noticeable mechanical difference between the two models in the pre-bifurcation stage.

Comparing Fig. 8(a) with Fig. 8(b), it is clear that the tensile strain in the soft phase does not directly affect on the global bifurcation point, but it has an effect on the strain distribution in the shear cohesive zone.

It is shown that the constant strain area also exists in the distribution of relative displacement in the shear cohesive zone, which is apparently different from the unlocalized crack model. The interesting phenomenon is that the shear strain of this constant strain area just corresponds to the critical displacement in cohesive law (5 nm) at the global bifurcation point. To show the difference of the two models more clearly, a statistic form of Fig. 8(b) is shown in Fig. 9.

From Fig. 9, we can describe the process of the crack initiation as a series of cohesive springs jumping over the critical point of the cohesive relationship. For the unlocalized mode, the strain distribution of the cohesive zone is more uniform, and the cohesive elements jump over the critical point one by one. For the localized mode, because of the constant strain area, when this large area of cohesive zone reaches the cohesive critical point, the entire system loses its stability abruptly, leading to a more localized crack initiation.

In this study, we successfully solved the fracture due to the micro-cracks in nacre and discussed the essential mechanisms of the transition between unlocalized and localized cracking modes. One of the newest finding in this research is the effect of the tensile behavior of soft phase on determination of cracking modes. It is believed that the mechanical property of soft phase only contributes to the shear adhesion in the conventional 'shear-lag model' (Jäger and Fratzl, 2000), and the behavior of soft phase in tensile deformation has been neglected in most of the previous studies. A recent experimental result (Slesarenko et al., 2017), however, shows that the mechanical properties of soft materials play an important role for micro-cracking of synthesized nacre-like composites. The research reveals the elastic modulus of soft matrix contributes to the overall strain hardening which is found in our present results.

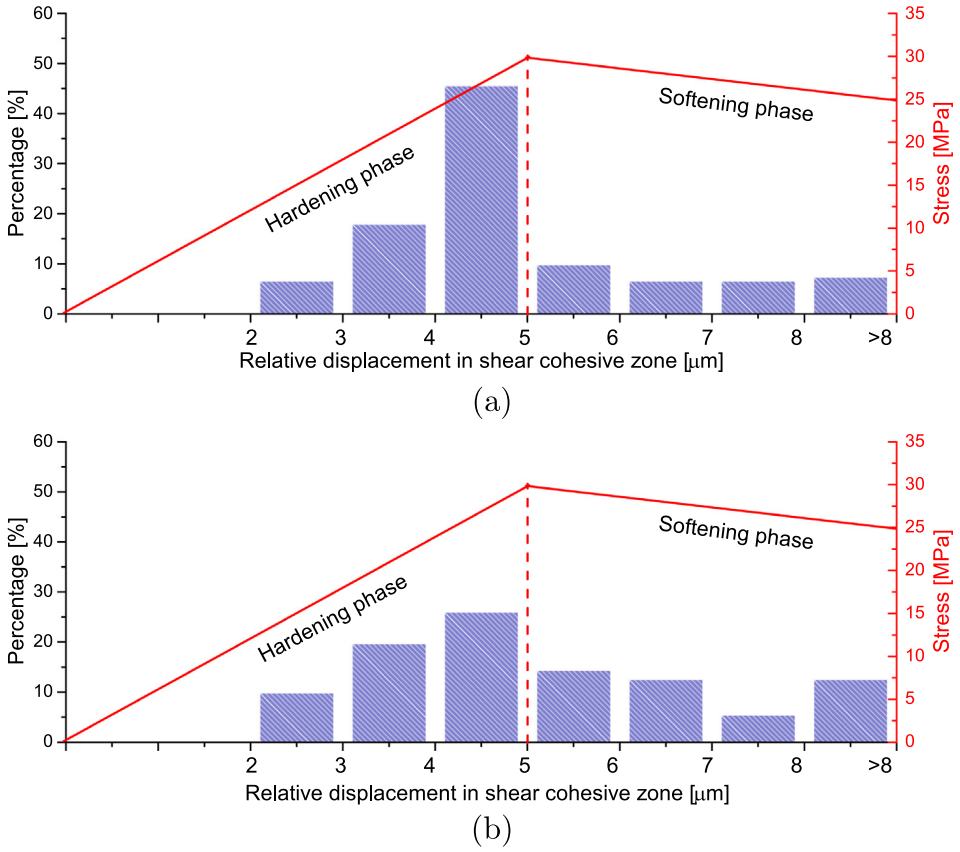

Fig. 9. Frequency distribution of the relative displacement in the shear cohesive zone at the bifurcation point: localized mode with standard parameters and unlocalized mode with $E_{soft} = 11.2$ GPa.

4. Conclusion

In this paper, we introduced two distinct crack modes in staggered biomaterials: localized mode and unlocalized mode. Systematic analysis has been conducted with regard to its mechanical behavior, quantitative characterization, intrinsic mechanism, and influencing factors.

In the localized crack mode, the crack initiates at a single position and also propagates near that position. In the unlocalized mode, several minor cracks initiates simultaneously or continuously. Using the crack localization factor, the two modes can be quantitatively distinguished. The two crack modes have completely different mechanical behaviors. Localized mode behaves closer to a brittle mechanical response. The stress rises to a high value at the beginning and then abruptly drops down after the crack initiation. On the contrary, the unlocalized mode has a more ductile mechanical response.

In order to find the intrinsic mechanism of the crack mode differentiation, we focused on the dynamic crack initiation process. Though the overall mechanical behaviors of the two modes are highly similar before the crack initiation, we have successfully grasped the intrinsic bifurcation point. The crack mode differentiation can be well explained by using the minimum energy functional principle in stability analysis.

Conflicts of interest

The authors have no conflicts of interest directly relevant to the content of this article.

Acknowledgements

The authors acknowledge financial support from the China Scholarship Council (granted number: 201606280019).

Appendix A. Supplementary material

Supplementary data associated with this article can be found, in the online version, at https://doi.org/10.1016/j.jbiomech.2019.02.003.

References

Abraham, F.F., 2001. The atomic dynamics of fracture. J. Mech. Phys. Solids 49, 2095–2111. https://doi.org/10.1016/S0022-5096(01)00028-X.

Allison, P.G., Moser, R.D., Chandler, M.Q., Rivera, O.G., Goodwin, J.R., Gore, E.R., Weiss Jr, C.A., 2015. Mechanical, thermal, and microstructural analysis of polyvinyl alcohol/montmorillonite nanocomposites. J. Nanomater., 2015 https://doi.org/10.1155/2015/291248.

An, B., Zhao, X., Arola, D., Zhang, D., 2014a. Fracture analysis for biological materials with an expanded cohesive zone model. J. Biomech. 47, 2244–2248. https://doi.org/10.1016/j.jbiomech.2014.04.054.

An, B., Zhao, X., Zhang, D., 2014b. On the mechanical behavior of bio-inspired materials with non-self-similar hierarchy. J. Mech. Behav. Biomed. Mater. 34, 8–17. https://doi.org/10.1016/j.jmbbm.2013.12.028.

Askarinejad, S., Rahbar, N., 2015. Toughening mechanisms in bioinspired multilayered materials. J.R. Soc. Interface, 12. https://doi.org/10.1098/rsif.2014.0855.

Askarinejad, S., Rahbar, N., 2018. Mechanics of bioinspired lamellar structured ceramic/polymer composites: experiments and models. Int. J. Plast. 107, 122–149. https://doi.org/10.1016/j.ijplas.2018.04.001.

Bargmann, S., Scheider, I., Xiao, T., Yilmaz, E., Schneider, G.A., Huber, N., 2013. Towards bio-inspired engineering materials: modeling and simulation of the

mechanical behavior of hierarchical bovine dental structure. Comput. Mater. Sci. 79, 390–401. https://doi.org/10.1016/j.commatsci.2013.06.028.
Barthelat, F., Tang, H., Zavattieri, P.D., Li, C.M., Espinosa, H.D., 2007. On the mechanics of mother-of-pearl: a key feature in the material hierarchical structure. J. Mech. Phys. Solids 55, 306–337. https://doi.org/10.1016/j.jmps.2006.07.007.
Barthelat, F., Espinosa, H.D., 2007. An experimental investigation of deformation and fracture of nacre-mother of pearl. Exp. Mech. 47, 311–324. https://doi.org/10.1007/s11340-007-9040-1.
Bigoni, D., 2012. Nonlinear Solid Mechanics: Bifurcation Theory and Material Instability. Cambridge University Press.
Borovik, A.V., Borovik, V.G., 2014. Effect of inelastic shear stress at the interfaces in the material with a unidirectional fibrous structure on the SIF for a crack in the fiber and the energy absorbed at fiber fracture. J. Mech. Behav. Biomed. Mater. 34, 75–82. https://doi.org/10.1016/j.jmbbm.2014.02.007.
Chintapalli, R.K., Breton, S., Dastjerdi, A.K., Barthelat, F., 2014. Strain rate hardening: a hidden but critical mechanism for biological composites? Acta Biomater. 10, 5064–5073. https://doi.org/10.1016/j.actbio.2014.08.027.
Cho, S.-S., Park, S., 2004. Finite element modeling of adhesive contact using molecular potential. Tribol. Int. 37, 763–769. https://doi.org/10.1016/J.TRIBOINT.2004.04.007.
Dastjerdi, A.K., Pagano, M., Kaartinen, M.T., McKee, M.D., Barthelat, F., 2012. Cohesive behavior of soft biological adhesives: experiments and modeling. Acta Biomater. 8, 3349–3359. https://doi.org/10.1016/j.actbio.2012.05.005.
Dubey, D.K., Tomar, V., 2009a. Role of the nanoscale interfacial arrangement in mechanical strength of tropocollagen-hydroxyapatite-based hard biomaterials. Acta Biomater. 5, 2704–2716. https://doi.org/10.1016/j.actbio.2009.02.035.
Dubey, D.K., Tomar, V., 2009b. The effect of tensile and compressive loading on the hierarchical strength of idealized tropocollagen-hydroxyapatite biomaterials as a function of the chemical environment. J. Phys. Condens. Matter: Inst. Phys. J. 21, 205103. https://doi.org/10.1088/0953-8984/21/20/205103.
Dubey, D.K., Tomar, V., 2009c. Understanding the influence of structural hierarchy and its coupling with chemical environment on the strength of idealized tropocollagen-hydroxyapatite biomaterials. J. Mech. Phys. Solids 57, 1702–1717. https://doi.org/10.1016/j.jmps.2009.07.002.
Dutta, A., Tekalur, S.A., 2014. Crack tortuousity in the nacreous layer – topological dependence and biomimetic design guideline. Int. J. Solids Struct. 51, 325–335. https://doi.org/10.1016/j.ijsolstr.2013.10.006.
Elices, M., Guniea, G.V., Gomez, J., Planas, J., 2002. The cohesive zone model: advantages, limitations and challenges. Eng. Fract. Mech. 69, 137–163. https://doi.org/10.1016/S0013-7944(01)00083-2.
Gautieri, A., Buehler, M.J., Redaelli, A., 2009. Deformation rate controls elasticity and unfolding pathway of single tropocollagen molecules. J. Mech. Behav. Biomed. Mater. 2, 130–137. https://doi.org/10.1016/j.jmbbm.2008.03.001.
Ghosh, P., Katti, D.R., Katti, K.S., 2007. Mineral proximity influences mechanical responses of proteins in biological mineral-protein hybrid systems. Biomacromolecules 8, 851–856. https://doi.org/10.1021/bm060942h.
He, M., Li, S., 2012. An embedded atom hyperelastic constitutive model and multiscale cohesive finite element method. Comput. Mech. 49, 337–355. https://doi.org/10.1007/s00466-011-0643-0.
Jäger, I., Fratzl, P., 2000. Mineralized collagen fibrils: a mechanical model with a staggered arrangement of mineral particles. Biophys. J. 79, 1737–1746. https://doi.org/10.1016/S0006-3495(00)76426-5.
Jiang, L.-Y., 2010. A cohesive law for carbon nanotube/polymer interface accounting for chemical covalent bonds. Math. Mech. Solids 15, 718–732. https://doi.org/10.1177/1081286510374548.
Launey, M.E., Buehler, M.J., Ritchie, R.O., 2010. On the mechanistic origins of toughness in bone. Annu. Rev. Mater. Res. 40, 25–53. https://doi.org/10.1146/annurev-matsci-070909-104427.
Launey, M.E., Munch, E., Alsem, D.H., Barth, H.B., Saiz, E., 2009. Designing highly toughened hybrid composites through nature-inspired hierarchical complexity. Acta Mater. 57, 2919–2932. https://doi.org/10.1016/j.actamat.2009.03.003.
Mayer, G., 2006. New classes of tough composite materials-Lessons from natural rigid biological systems. Mater. Sci. Eng., C 26, 1261–1268. https://doi.org/10.1016/j.mSection 2005.08.031.
Munch, E., Launey, M.E., Alsem, D.H., Saiz, E., Tomsia, A.P., Ritchie, R.O., Tanay, A., Bitincka, L., Shamir, R., Shea, E.K.O., Tschumi, A.I., Kishony, R., Telmer, C.A., Adler, S.A., Subramaniam, V., Lopez, A.J., Mitchison, T.J., Perrimon, N., Fraser, S.E., Ellenberg, J., Lamond, A.I., Brotman, J.S., Sweeney, S.T., Davis, G., Daneman, R., Zavortink, M., Chia, W., Liu, L.F., Arpa, P.D., Pfund, W.P., Mehta, V.B., Trask, D.K., Makonchuk, D., Gomes, C., Zheng, J.J., Hetman, M., Wold, M.S., Borowiec, J.A., Elston, T.C., Blake, W.J., Collins, J.J., Levine, A.J., Siggia, E.D., Swain, P.S., Thattai, M., Kurtser, I., Grossman, A.D., Oudenaarden, A.V., Arlander, S.J., Karnitz, L., Lin, C., Sun, S.Y., Zhao, S., Liu, Z.R., Old, W.M., Resing, K.A., Ahn, N.G., Mann, M., Bar, J., Glinert, I., Shlapok, T., Munch, E., Launey, M.E., Alsem, D.H., Saiz, E., Tomsia, A.P., Ritchie, R.O., 2008. Tough, bio-inspired hybrid materials. Science 322, 1516–1520. https://doi.org/10.1126/science.1164865.
Needleman, A., 2013. Some issues in cohesive surface modeling. Procedia IUTAM 10, 221–246. https://doi.org/10.1016/j.piutam.2014.01.020.
Niebel, T.P., Bouville, F., Kokkinis, D., Studart, A.R., 2016. Role of the polymer phase in the mechanics of nacre-like composites. J. Mech. Phys. Solids, 96. https://doi.org/10.1016/j.jmps.2016.06.011.
Scheider, I., Xiao, T., Huber, N., Mosler, J., 2013. On the interaction between different size effects in fibre reinforced PMMA: towards composites with optimised fracture behaviour. Comput. Mater. Sci. 80, 35–42. https://doi.org/10.1016/j.commatsci.2013.04.027.
Scheider, I., Xiao, T., Yilmaz, E., Schneider, G.A., Huber, N., Bargmann, S., 2015. Damage modeling of small-scale experiments on dental enamel with hierarchical microstructure. Acta Biomater. 15, 244–253. https://doi.org/10.1016/j.actbio.2014.11.036.
Shao, Y., Zhao, H.-p., Feng, X.-q., 2012. Discontinuous crack-bridging model for fracture toughness analysis of nacre. J. Mech. Phys. Solids 60, 1400–1419. https://doi.org/10.1016/j.jmps.2012.04.011.
Shao, Y., Zhao, H.-p., Feng, X.-q., 2014. On flaw tolerance of nacre: a theoretical study. J. Roy. Soc. Interface/Roy. Soc. 11, 20131016. https://doi.org/10.1098/rsif.2013.1016.
Slesarenko, V., Volokh, K.Y., Aboudi, J., Rudykh, S., 2017. Understanding the strength of bioinspired soft composites. Int. J. Mech. Sci., 171–178 https://doi.org/10.1016/j.ijmecsci.2017.06.054.
Tvergaard, V., Hutchinson, J.W., 1992. The relation between crack growth resistance and fracture process parameters in elastic-plastic solids. J. Mech. Phys. Solids 40, 1377–1397. https://doi.org/10.1016/0022-5096(92)90020-3.
Wang, R., Gupta, H.S., 2011. Deformation and fracture mechanisms of bone and nacre. Annu. Rev. Mater. Res. 41, 41–73. https://doi.org/10.1146/annurev-matsci-062910-095806.
Wegst, U.G.K., Ashby, M.F., 2004. The mechanical efficiency of natural materials. Philos. Mag. 84, 2167–2181. https://doi.org/10.1080/14786430410001680935.
Wegst, U.G.K., Bai, H., Saiz, E., Tomsia, A.P., Ritchie, R.O., Ortiz, C., Boyce, M., Wegst, U.G.K., Bai, H., Saiz, E., Tomsia, A.P., Ritchie, R.O., 2014. Bioinspired structural materials. Nat. Mater. 14, 23–36. https://doi.org/10.1038/nmat4089.
Xie, Z., Yao, H., 2014. Crack deflection and flaw tolerance in brick-and-mortar structured composites. Int. J. Appl. Mech. 06, 1450017. https://doi.org/10.1142/S1758825114500173.
Yahyazadehfar, M., Arola, D., 2015. The role of organic proteins on the crack growth resistance of human enamel. Acta Biomater. 19, 33–45. https://doi.org/10.1016/j.actbio.2015.03.011.